The paper was published in the proceedings of the 11th International Conference on Physical Modelling in Geotechnics (ICPMG2026) and was edited by Ioannis Anastasopoulos. The conference was held from June 8th to June 12th 2026 in Zurich, Switzerland.

A centrifuge dam-break wave generator: development and measurements

A. Mink
University of Colorado Boulder, Boulder, USA, angela.mink@colorado.edu

S. S. C. Madabhushi
University of Colorado Boulder, Boulder, USA, mscs@colorado.edu

ABSTRACT: Fluid-soil-structure interaction (FSSI) underpins the performance of coastal infrastructure but remains challenging to experimentally study due to the coupling of geotechnical and hydraulic processes. Large-scale wave flumes can have long horizontal extents to model natural wave propagation and attenuation but are often limited in terms of the soil depth that can be modeled. By contrast, geotechnical centrifuge models can recreate large depths of soil but are likely more limited in terms of recreating long period waves. The current study presents a recently developed dam-break wave generator, compatible with the University of Colorado Boulder's 400 g-ton centrifuge, to explore FSSI under extreme wave loads. An overview of the equipment design is first given. Following this, illustrative interpretations of fluid pressure and pore pressure measurements at the soil surface and at depth are shown, as well as a comparison to wave-height tracking obtained from a high-speed camera. These comparisons motivate careful interpretation of the gravimetric, hydrodynamic, and other transient components of the pore pressures induced by the propagating water wave. Finally, total head distributions and excess pore pressure time histories are calculated to inform evolving strength changes in soil. Broadly, the present study informs measurement and interpretation techniques for future FSSI centrifuge studies.

1 INTRODUCTION

The resilience of coastal cities can strongly depend on the performance of their infrastructure during destructive wave events. Coastal storms as well as seismic activity offshore present risks of ocean surges and large waves along the coastline. In the notable 2022 Hurricane Ian, ocean surges of up to 4.5 m inundated the southwest coast of Florida, causing a tremendous $112.9 billion in damage and claiming 156 lives (Bucci et al., 2023). Protective infrastructure such as seawalls and breakwaters can lessen the effects of natural disasters, but these, along with inland structures, must be carefully designed to withstand the hydrodynamic loads imposed on them. A structure's response to wave loading can be understood through the interaction between the structure, the water, and the soil supporting the structure. This fluid-soil-structure interaction (FSSI) can be critical but is difficult to model and observe. The current study introduces recently developed physical modeling equipment compatible with the University of Colorado (CU) Boulder's 400 g-ton centrifuge that seeks to capture hydraulic, structural, and geotechnical phenomena during destructive wave loading.

Conventionally, large wave basin facilities have been a common experimental approach in coastal engineering research. For example, the wave basins at Oregon State University (OSU) enabled study of horizontal wave forces on elevated structures (Tomiczek et al., 2019) and the run-up variability dependent on different wave group characteristics (Li et al., 2022). Li and Gao (2022) conducted a study focused on the spatio-temporal propagation of excess pore pressure through a soil depth during wave loading and derived a nondimensional term based on wave and soil characteristics to describe it. Although these studies involve specially engineered waves that can propagate naturally along the flume's length, they often have limited soil depths (e.g., between 0.3-0.5 m). Geotechnical responses critical to understanding FSSI cannot be reliably captured in shallow 1-g experiments, thus motivating centrifuge modeling to replicate in-situ stress conditions and accurately observe fluid-soil-structure behavior. An illustrative comparison between the dimensions of OSU's large-scale wave flume and those of the presented centrifuge model is shown in Figure 1.

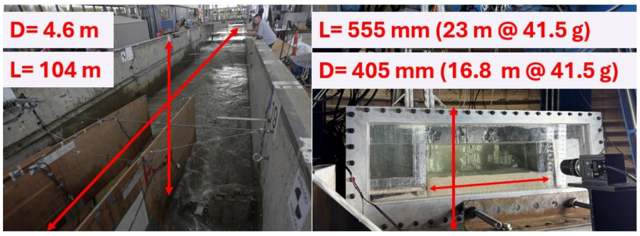

Figure 1. OSU wave flume (left) and CU's wave box (right) with respective length and depth. Dimensions of CU's wave box are reported at model and prototype scale at 41.5g.

Previous centrifuge modeling studies of FSSI include Takahashi et al. (2014) who studied steady state seepage around a breakwater and later, modeled tsunami inundation in a centrifuge (Takahashi et al., 2019). Exton et al. (2018) also constructed a centrifuge tsunami generator, simulating runup and drawdown of a wave over a bed of sand. They eventually used this equipment to study the effects of an impermeable layer, such as pavement, on the effective stresses within the soil beneath this layer, finding that the impermeable layer sustained excess pore pressures and could drive soil instability (Exton and Yeh, 2022).

However, there are still significant gaps in the knowledge of hydrodynamic and consolidation processes that occur within the soil and around coastal structures during a wave event. In particular, the timing of these mechanisms and their respective influence on soil strength are not yet well resolved. Using CU's 400 g-ton centrifuge and the experimental set-up described herein, insights into pore pressures and soil strength throughout extreme wave events are provided to set the stage for experiments to improve engineering designs of a broad range of coastal infrastructure systems.

2 METHODOLOGY

2.1 Centrifuge scaling laws

The model was constructed to be scaled by a factor of N = 41.5. Powered by a 670 kW motor, the largest centrifuge at CU Boulder has a 5.5 m long arm on the platform side and accommodates the dam-break wave generator: an assembly of a 40 cm × 100 cm × 50 cm soil container and gate apparatus.

Scaling laws for the soil body are well established in the practice of centrifuge modeling. However, achieving dynamic similitude in moving fluids is more challenging. Hydrodynamic similarity across scales involves matching both the Reynolds number, which governs the transition between laminar and turbulent flow, and the Froude number, which represents the balance of inertial and gravitational forces. On the other hand, reproducing diffusive processes within the soil bed requires matching Terzaghi's number (T_z), defined by Equation 1, where u_e is excess pore pressure and t is time.

$$\frac{\partial u_e}{\partial t} = T_z \nabla^2 u_e \qquad (1)$$

While the dynamic viscosity of the model fluid can be increased to match dynamic and diffusive timescales, doing so would further distort the Reynolds number (Exton and Yeh, 2022). The centrifuge experiments presented herein did not explicitly scale the grain size or fluid viscosity. As a result, the model-scale diffusion velocities are $N \times$ greater than the field-scale diffusion velocities. For simplicity, the current study will present measurements at the model-scale time as pore pressure changes due to dynamic versus diffusive processes are not easily decoupled. Future work will focus on best experimental and interpretation techniques to resolve potential time-scaling discrepancies which will allow these results, and FSSI more broadly, to be better mapped to field scales.

Table 1. Summary of key scaling laws for hydraulic processes, following Exton and Yeh, 2022.

Scale	**(model/field)**
Froude Number, F_r	1
Reynolds Number, R_e	1/N
Terzaghi Number, T_z	N/1
Velocity (dynamic)	1
Velocity (diffusive/consolidation)	N/1
Time (dynamic)	1/N
Time (diffusive/consolidation)	$1/N^2$

2.2 Box, instrumentation, and soil

An approximately 10 cm thick plexiglass window was integrated along one side of a rigid container to provide clear visualization of the wave cross-section as well as soil and structure displacements. The container and gate apparatus are shown in Figure 2. A pneumatic actuator was mounted directly above a gate that holds back a 0.0183 m^3 reservoir of fluid. The gate is opened in-flight to generate the dam-break wave, opening in an average 0.04 s when the actuator is supplied with 800 kPa of air pressure from an accumulator. To minimize unwanted reflections, an empty downstream catch pot was incorporated to capture overtopping water. In theory, this reduces reflections above the catch pot height. However, reflections below its top, including pore fluid movement within the soil, are inevitable in the rigid container. The reduced ability to mitigate wave reflections is noted as a drawback of the present centrifuge model, in contrast to the dissipation techniques commonly applied in large wave flumes. The analysis presented in this paper focuses on the first wave as it partially propagates the length of the box and assumes the observed fluid and soil behavior are relatively unaffected by reflections during this time window.

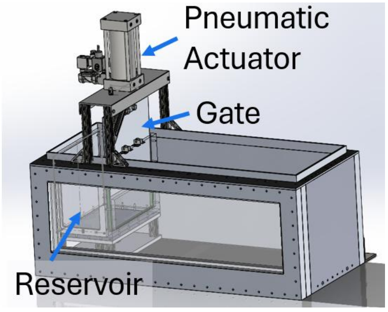

Figure 2. SolidWorks rendering of soil container with attached gate apparatus.

Instrumentation included a high-speed camera recording at 1000 fps and an array of pore pressure transducers (PPTs). The PPTs were fabricated in-house using MS5407 analog sensors with porous stainless-steel disks, broadly following the method of Jacobsz (2018). They were submerged and calibrated under pressure and relative vacuum conditions over a range of –15 to 400 kPa to ensure the sensors can withstand the anticipated fluid pressures in the centrifuge. During the experiments, pressure data was recorded at a sampling rate of 5000 Hz. Slower sampling frequencies (100 Hz) were used during spin up and spin down to observe any events that could occur during that time such as a PPT moving or foundation settlement.

In this paper, the results from two centrifuge tests are discussed. The geometries of the soil and initial hydraulic conditions were largely similar, with the key differences being the inclusion of a shallow foundation and altered PPT placement in the second test. The Ottawa F-65 soil deposit was pluviated using an automatic sand pourer in several sublayers to achieve an average dry density of 14.7 kN/m^3 and a void ratio of 0.77, i.e., very loose sand (D_r = 5 %). PPTs were placed in between layers throughout the pluviation, in the arrangement shown in Figure 3. Sensors were oriented either to face the incoming wave directly (normal to the wave velocity) or, alternatively, to align parallel with the wave's direction of travel. This approach was intended to quantify hydrodynamic pressures generated by pore-fluid accelerations. Differences between the two sensor orientations were found to be negligible in the experiments presented; therefore, PPTs in different orientations will be treated equivalently.

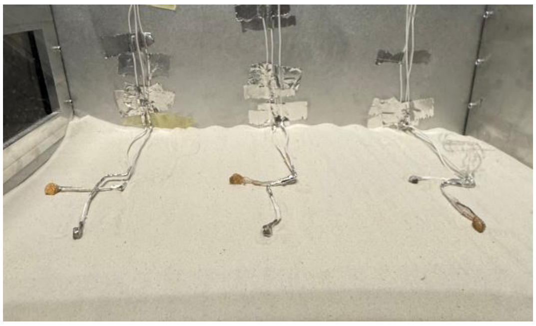

Figure 3. PPTs oriented normal to the wave direction (front row) and parallel to the wave direction (back row)

A stainless-steel block, representing a rigid shallow foundation, was included in the second test and was placed in the same fashion as the PPTs; pluviating the final layers around the foundation until its surface was level with the soil's. A map of the approximate PPT and foundation location is shown in Figure 4. Every blue PPT exists in both Test 1 and 2, while the red PPTs and the foundation were added only for Test 2. The initial water depth above the soil surface was 120mm (4.8 m prototype scale) in Test 1 and 100 mm (4.2 m prototype scale) in Test 2.

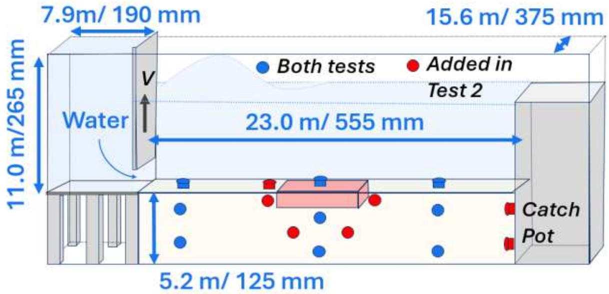

Figure 4. Instrumentation layout and model footing in Test 1 and 2. Dimensions are reported as prototype scale/model scale (with N=41.5g).

3 ILLUSTRATIVE RESULTS

In both tests, time histories of PPTs along the soil surface reflect the pressure increases and decreases expected with the passage of a wave. Figure 5 shows the pressure increase above the initial hydrostatic conditions with time in Test 2. Note that these time histories are filtered below 80 Hz to isolate the general trend of pressure changes due to the wave in prototype scale. This plot is used to illustrate the assumption that significant wave reflections do not begin in the free fluid before the peak wave height is reached at the PPT furthest from the gate. The oscillation in PPT A's pressure (i.e., the blue line) can be attributed to a small vortex within the free fluid caused by turbulent mixing between the water being released from the reservoir and the initially still water table above the soil.

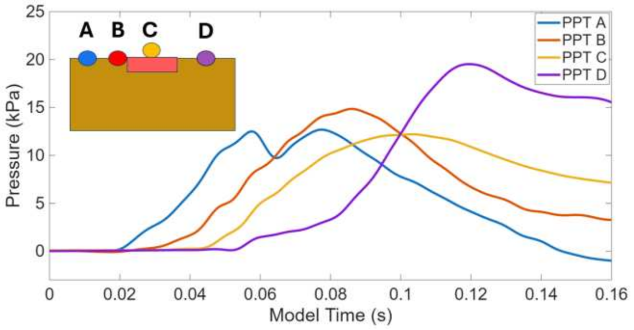

Figure 5. Surface pressure trends along the length of the soil deposit due to the wave increasing the water height at each location.

To understand the hydraulic processes above and within the soil, it is necessary to decipher hydrostatic from hydrodynamic pressures recorded by the sensors. Here, evaluating the recorded pressure components involves a comparison between wave height calculated from surface PPT data and wave height measured with a video tracking software called *Tracker* (Brown 2009). To enable direct comparison, wave heights are calculated at the model scale using the equation below where h_w is the height of water above the soil surface, P is the pressure recorded by the PPT in units of kPa, N is the centrifuge scale factor (in this case, 41.5), and γ_{water} is the unit weight of water (9.81 kN/m^3).

$$h_w = \frac{P}{N * \gamma_{water}} \qquad (2)$$

The wave height comparison is shown in Figure 6 and reveals a broad similarity of the wave shape but with a significantly different high-frequency component captured by the PPTs. The sensors are inferred to measure a hydrostatic pressure (i.e., due to gravity acting on the changing fluid height) along with hydrodynamic pressures caused by vertically accelerating water in a vortex, e.g., as shown in the photograph in Figure 6. Applying a low-pass filter with a cutoff at 80 Hz (model time scale) to the surface PPT data yields a close approximation of the wave heights, and by extension, hydrostatic pressure along the length of the model at any given time. This verification is valuable because it allows delineation of the component of subsurface pore-pressure measurements that can be attributed to hydrostatic pressure (i.e., the wave height) versus dynamic effects.

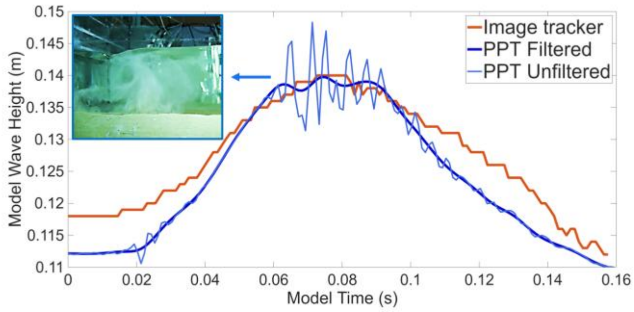

Figure 6. Wave height calculated from surface pressures versus measured with tracking software. Unfiltered data reflects the turbulence caused by the vortex.

Following the above results for the wave released over a level soil deposit (Test 1), the development of pore pressures when a shallow foundation is embedded in the soil are now considered (Test 2). Total head distributions are useful illustrations that help reveal transient patterns of the pore fluid pressure. Total head (h_T) will be described as the sum of three energy components: gravitational potential energy (h_Z), kinetic energy (h_V) and pressure energy (h_P). By setting the elevation datum at the initial water surface, the exact vertical position of each sensor—equivalent to h_Z at the prototype scale—is calculated from initial hydrostatic pressures. The pressure is continuously recorded throughout the duration of the wave, informing the value of h_P, which can be defined by the following equation, where P is the recorded pressure in kPa and γ_{water} is 9.81 kN/m^3.

$$h_P = \frac{P}{\gamma_{water}} \qquad (3)$$

Measured pressures between PPTs oriented normal and parallel to the wave direction were nearly identical, so h_V was deemed negligible. This notation, with the datum set at the initial water surface, results in the initial total head having a value of zero everywhere in the soil. This is because h_Z is the negative value of h_P under hydrostatic conditions. It is expected that as the water height rises above the datum during the wave, total head will increase in the soil.

The total head is calculated at the location of PPTs and linearly interpolated between them wherever there is soil. Corresponding wave profiles are calculated from filtered surface PPT data following Figure 6, such that they describe the height of the wave above the original water surface along the length of the box and ignore oscillating hydrodynamic pressures. The resulting total head distributions and wave profiles are shown at three different model times in Figure 7.

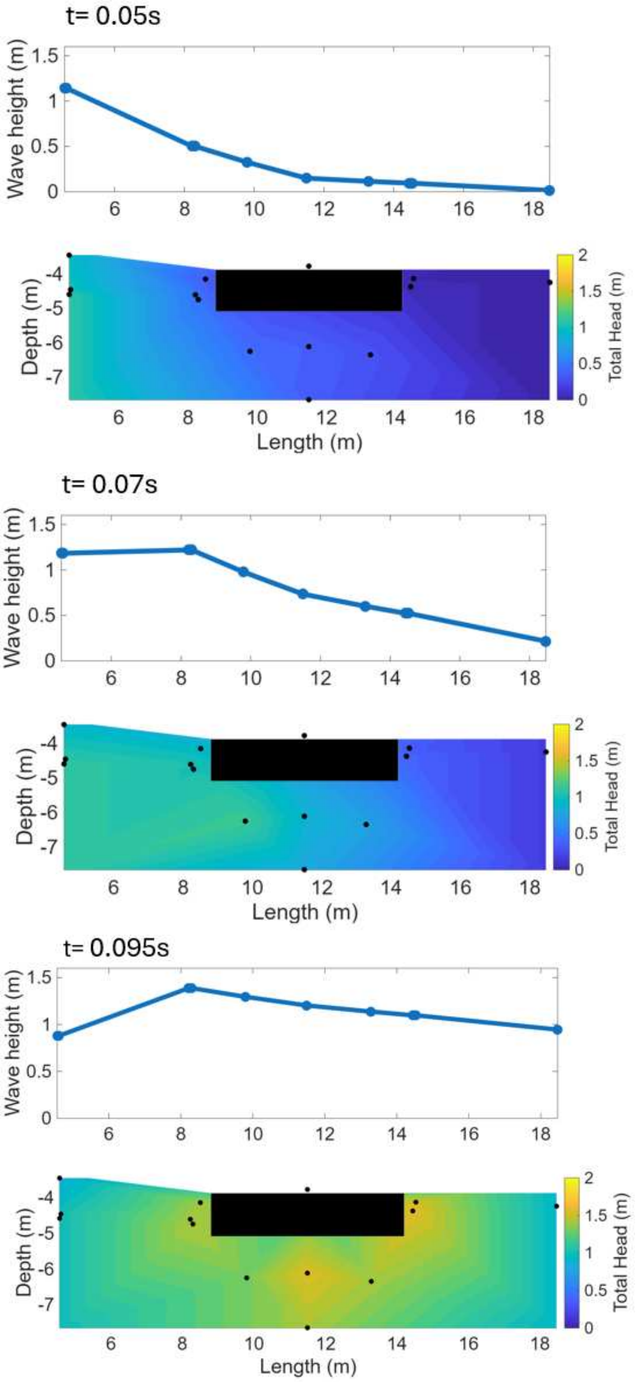

Figure 7. Wave profiles (prototype scale) and corresponding total head (h_T) contours over a prototype scale grid at model times: 0.05 s, 0.07 s, and 0.095 s. Black markers represent PPTs.

As expected, Figure 7 shows total head increases within the soil as the wave propagates overhead. While the wave is clearly not a steady state event, the total head gradients could inform temporary flow regimes of the pore fluid. Note that if pore pressures in the soil increase solely due to an increase in wave height and hence hydrostatic pressure, the total head values within the soil will reflect the same change as the wave height. However, Figure 7 often reveals values of h_T greater than the wave height ahead of the wave crest and around the foundation. The mismatch between h_T and wave height shows that processes beyond hydrostatic pressure drive the measured pore pressure response.

Examining the time histories of pore pressures in the soil versus vertically aligned surface pressures informs the interpretation of developing excess pore pressures, u_e. Pressure deviations from the initial hydrostatic condition at each PPT location are shown in Figure 8 to highlight discrepancies between the free fluid and the pore fluid response at different locations.

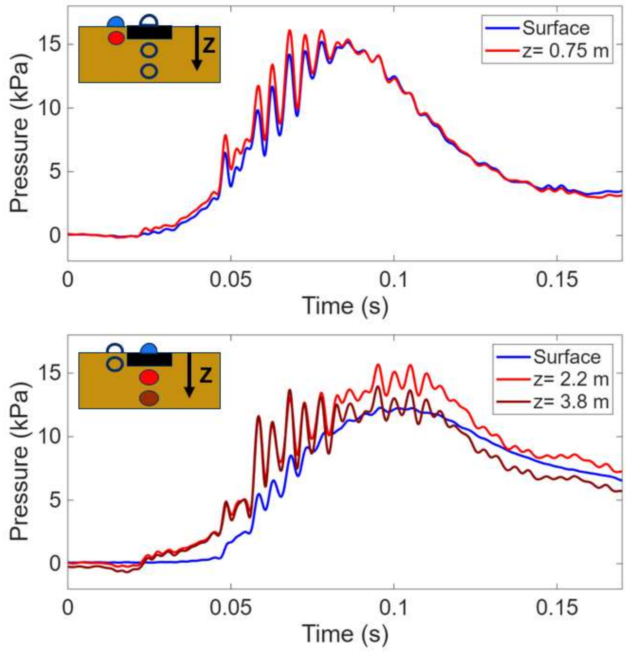

Figure 8. Pressure–time histories at different locations in the soil during wave loading. Time is shown in model scale, depth (z) is in prototype scale.

In the top panel of Figure 8, the dynamic and static pressures at the surface are transmitted directly to the shallow PPT. Hydrostatic pressures rise and fall simultaneously, and minor dynamic oscillations remain in phase between the surface and the shallow PPT.

By contrast, the bottom panel of Figure 8 shows hydrostatic pressures below the foundation rising before the local water level rises from the incoming wave. This suggests that pressures induced by the wave at the left end of the surface are transmitted through the soil to the pore fluid ahead of the wave crest. Dynamic oscillations also appear to be in phase between the foundation surface and deeper PPTs, but the amplitudes of pressure spikes are much larger in the soil. The large spikes can be explained by either (1) superposition of pressure waves arriving from the nearby soil and the surface of the foundation or (2) excess pore pressure generated during oscillating dynamic pressures on the rigid foundation.

While the pore pressures appear to respond to both the free fluid and neighboring soil regions, the hydrostatic and dynamic pressures at the surface are taken to be fully transmitted through the entire soil depth. This motivates the assumption that all components of surface pressures directly impact changes in the soil's total stress but do not inherently change the effective stress if pore pressures change in the same fashion. Therefore, u_e is defined as the difference between the change in pore pressure, u_p, and the change in pressure imposed at the soil surface by the free fluid, u_f, as described by Equation 4.

$$u_e = (u_p - u_{p0}) - (u_f - u_{f0}) \qquad (4)$$

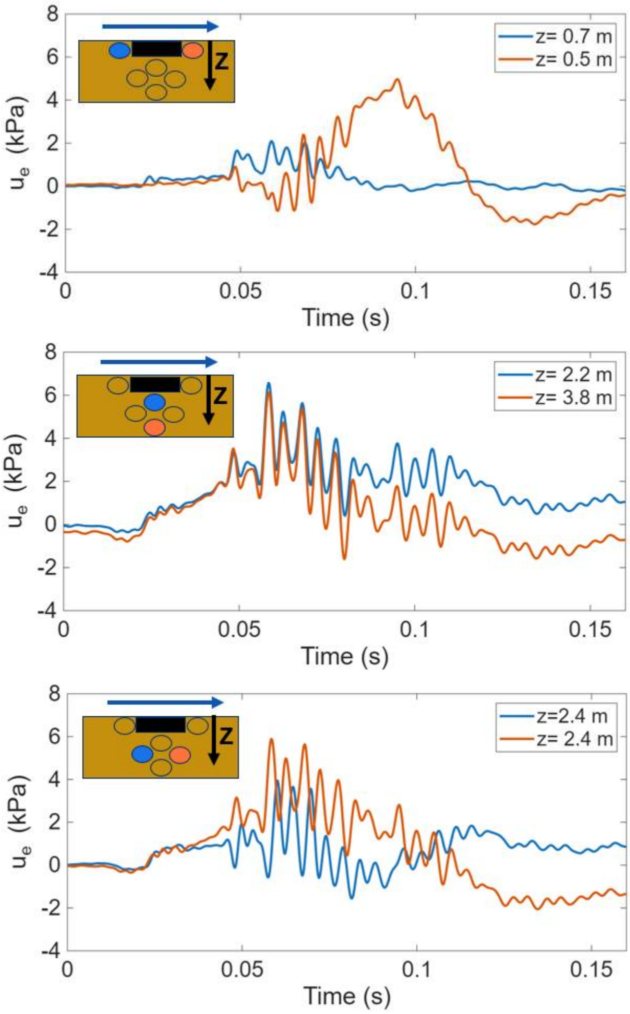

Figure 9. Development of u_e throughout one wave cycle. The blue arrow depicts the direction of the wave. Time is at the model scale and depth dimensions are at the field scale.

Following this interpretation, excess pore pressures are presented in Figure 9. The oscillations observed in the u_e time history are most obvious beneath the foundation, where hydrodynamic loading is potentially encouraging volumetric strain in the soil. However, the residual excess pore pressures (i.e., u_e remaining after the wave passes) are negligible as the loose sand behaves in a drained manner. With a fine grained sand at a relative density of 60%, Sassa and Sekiguchi (1999) observed liquefaction due to residual excess pore pressure at shallow depths (z = 0.5 m, prototype scale) after only 5 wave cycles. By contrast, the equipment presented herein is geared towards modeling the soil-structure response to one large destructive wave, informing the mechanisms leading to the development of momentary soil weakening during solitary wave events like tsunamis.

The excess pore pressure trends observed in Figure 9 are complex, and decoupling the underlying mechanisms requires further study. Nevertheless, a combination of transient pore pressures and soil-structure interaction provides a useful framework for interpreting the soil response within the model.

As the wave enters from the left, hydrostatic pressure increases quickly beneath the wave front, potentially sending a compressional wave through the soil to neighboring areas faster than the wave crest travels at the surface. This can explain the gradual increase in u_e below the foundation, especially between time 0 s and 0.05 s, as Figure 8 shows the initial increase of u_p occurring before the wave front reaches the foundation.

Further, an FSSI perspective inspires the hypothesis that hydrodynamic pressure oscillations imposed on the foundation tend to induce volumetric soil strain, accounting for the high frequency oscillations in u_e observed below the foundation. A combined sliding and rotational motion of the foundation may also explain the u_e measured in the embedment to the right of the foundation (z = 0.5 m). The accumulation of u_e beneath the right corner of the foundation (z = 2.4 m), and its magnitude compared to the left corner, indicates a rotational motion of the foundation.

Across the soil domain, positive excess pore pressures and corresponding reductions in vertical effective stress occur during the wave event. Variations of up to 8 kPa are transmitted to the soil skeleton, potentially resulting in significant strength changes in the modeled soil depth. The observed cyclic nature of pore pressure and effective stress fluctuations also raises concerns regarding accumulated volumetric strains (i.e., foundation failure). Overall, the fluid–soil interactions observed in Test 2 demonstrate potential challenges to coastal infrastructure performance, with the magnitude and timing of these effects warranting further investigation.

4 CONCLUSIONS

The design and capabilities of a dam-break wave generator for CU Boulder's 400 g-ton centrifuge were introduced. Preliminary results from two tests are also discussed, emphasizing the interpretation of the free-fluid and pore fluid pressures. The potential for rapid wave reflections within the soil is noted as a drawback of the centrifuge model when compared to a longer wave flume, while being able to observe soil behavior at depths relevant to coastal FSSI is a key advantage.

Wave tracking with PPT time histories as well as high-speed image tracking revealed both hydrostatic and hydrodynamic pressure components measured by the sensors at the soil surface that a pure imaging technique would miss. From here, tracking of wave height and total head distributions with time revealed that soil-fluid processes during the event modeled were not merely hydrostatic. While decoupling the mechanisms within the soil requires further study, insights are made based on the movement of pore fluid in the soil (i.e., FSI) and the interaction with the foundation (i.e., FSSI). The magnitude of measured excess pore pressures and cycling indicate a potential for soil weakening throughout the duration of the wave.

Overall, several insights and future directions for FSSI are inspired by the present study. Broadly, the equipment developed is anticipated to be a valuable tool to explore the performance of coastal infrastructure, and in particular, representative changes of soil strength and stiffness due to phenomena such as transient pore pressures and/or mechanically induced excess pore pressures.

ACKNOWLEDGEMENTS

The first author would like to acknowledge the personal and technical support from Prof. Madabhushi's *Boulder Geomechanics and Geohazards* research group. The contributions from the CIEST staff, in particular John Hindman, were crucial to develop the equipment and instruments and execute these tests.

REFERENCES

Bucci, L., Alaka, L., Hagen, A., Delgado, S., & Beven, J. (2023). *Tropical Cyclone Report: Hurricane Ian (AL092022), 23–30 September 2022*. National Hurricane Center. Retrieved December 2025. https://www.nhc.noaa.gov/data/tcr/AL092022_Ian.pdf

Brown, D. (2008). Video Modeling: Combining Dynamic Model Simulations with Traditional Video Analysis. Paper presented at AAPT 2008 Summer Meeting, Edmonton, Alberta. Retrieved February 2026. https://www.compadre.org/Repository/document/ServeFile.cfm?ID=7844&DocID=633

Exton, M. C., Harry, S., Mason, H. B., Yeh, H., & Kutter, B. L. (2018). *Novel experimental device to simulate tsunami loading in a geotechnical centrifuge*. CRC Press.

Exton, M., & Yeh, H. (2022). Effects of an impermeable layer on pore pressure response to tsunami-like inundation. *Proceedings of the Royal Society A: Mathematical, Physical and Engineering Sciences*, *478*(2257). https://doi.org/10.1098/rspa.2021.0605

Jacobsz, S. W. (2018). Low cost tensiometers for geotechnical applications. In McNamara et al. (Ed.), *International Journal of Physical Modelling in Geotechnics*. Taylor & Francis Group.

Li, C. F., & Gao, F. P. (2022). Characterization of spatio-temporal distributions of wave-induced pore pressure in a non-cohesive seabed: Amplitude-attenuation and phase-lag. *Ocean Engineering*, *253*. https://doi.org/10.1016/j.oceaneng.2022.111315

Li, C., Özkan-Haller, H. T., Lomonaco, P., Maddux, T. B., & García-Medina, G. (2022). Experimental Study of Wave Runup Variability on a Dissipative Beach. *Journal of Geophysical Research: Oceans*, *127*(6). https://doi.org/10.1029/2022JC018418

Sassa, S., & Sekiguchi, H. (1999). Wave-induced liquefaction of beds of sand in a centrifuge. *Geotechnique*, *49*(5), 621–638. https://doi.org/10.1680/geot.1999.49.5.621

Takahashi, H., Morikawa, Y., & Kashima, H. (2019). Centrifuge modelling of breaking waves and seashore ground. *International Journal of Physical Modelling in Geotechnics*, *19*(3), 115–127. https://doi.org/10.1680/jphmg.17.00037

Takahashi, H., Sassa, S., Morikawa, Y., Takano, D., & Maruyama, K. (2014). Stability of caisson-type breakwater foundation under tsunami-induced seepage. *Soils and Foundations*, *54*(4), 789–805. https://doi.org/10.1016/j.sandf.2014.07.002

Tomiczek, T., Wyman, A., Park, H., & Cox, D. T. (2019). Modified Goda Equations to Predict Pressure Distribution and Horizontal Forces for Design of Elevated Coastal Structures. *Journal of Waterway, Port, Coastal, and Ocean Engineering*, *145*(6). https://doi.org/10.1061/(asce)ww.1943546 0.0000527